Frictional Properties on the San Andreas Fault near Parkfield, California, Inferred from Models of Afterslip following the 2004 Earthquake

by Kaj M. Johnson, Roland Bürgmann, and Kristine Larson

Abstract   The abundance of geodetic and seismic data recording postseismic deformation following the 2004 Parkfield earthquake provides an unprecedented opportunity to resolve frictional properties on the Parkfield section of the San Andreas fault. The Parkfield segment is a transition between the locked section to the southeast that last ruptured in the 1857 Fort Tejon earthquake and the creeping section to the northwest. We develop three-dimensional rate- and state-dependent friction models of afterslip following the 2004 earthquake to investigate the frictional behavior of the fault. It is assumed that the coseismic rupture occurred on an area of the fault surrounded by aseismic creep that accelerated after the earthquake. We estimate the distribution of coseismic slip, afterslip, and rate–state frictional parameters by inverting a two-step slip model. In the model we (1) estimate the coseismic slip distribution from 1-Hz Global Positioning System (GPS) data and (2) use the corresponding coseismic shear stress change on the fault as input into a numerical afterslip model governed by rate–state friction. We find the rate–state frictional parameter A–B, an indicator of frictional stability, is in the range 10^{-4}–10^{-3} at 50 MPa normal stress, which is near the transition from potentially unstable (negative A–B) to nominally stable (positive A–B) friction. The estimate of A–B values falls within a wide range of experimental values reported for serpentinite, which crops out along the San Andreas fault zone. The critical slip distance, d_c, which characterizes the distance over which strength breaks down during a slip event, is in the range 0.01–0.1 m, consistent with seismic estimates and a fault gouge thickness of 1–10 m. The afterslip model reproduces most features observed in the GPS time-series data including high surface velocities in the first few months after the earthquake and lower rates at later times, as well as the cumulative postseismic displacement. The model tends to underpredict the displacement data at later times, suggesting that perhaps the modeled afterslip period ends too quickly or an unmodeled deformation process dominates the signal at later times.

Introduction

Although the 28 September 2004 **M** 6.0 Parkfield earthquake was only a moderate size event, the abundance of geophysical instrumentation at Parkfield provides an unprecedented opportunity to study the physics governing slip on the fault. Arrays of Global Positioning System (GPS) receivers, creepmeters, strainmeters, borehole seismometers, and strong ground motion instruments all located near the fault make the Parkfield event one of the best observed earthquakes to date (Langbein *et al.*, 2005).

The Parkfield section of the San Andreas fault is transitional between creeping and locked sections (Fig. 1). The fault creeps about 25 mm/yr (Murray *et al.*, 2001) to the northwest and is locked to the southeast along the section that last ruptured in the **M** 7.9 1857 Fort Tejon earthquake. Within the Parkfield transition zone, the fault displays both stick-slip and stable sliding behaviors. The 2004 earthquake is the latest in a well-known sequence of **M** ~6 events.

Numerous observations point to a model for the Parkfield section of a locked patch, or asperity, surrounded by aseismic creep (e.g., Boatwright and Cocco, 1996; Murray *et al.*, 2001; Segall and Harris, 1986). The locked patch is roughly outlined by the relocated seismicity before and after the 2004 earthquake (Fig. 1). This inferred locked patch presumably ruptures in the **M** ~6 earthquake sequence as suggested by slip inversions for the 2004, 1966, and 1934 earthquakes, which ruptured similar but not identical portions of
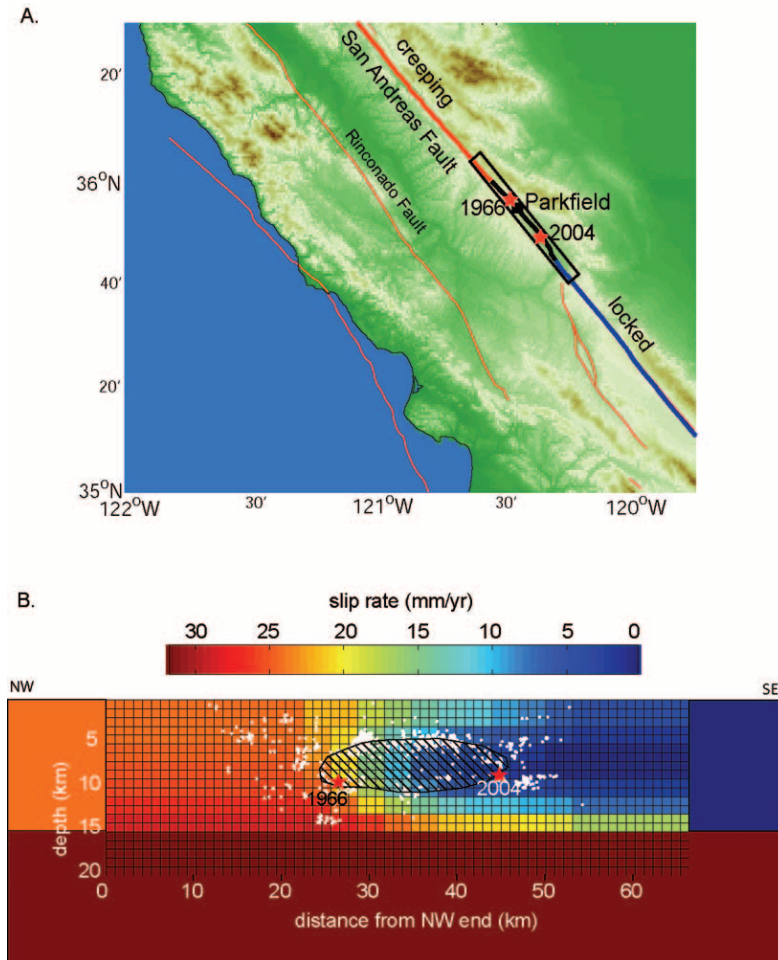
A.

B.

Figure 1.   (A) Location of the Parkfield segment of the San Andreas fault. The box on the San Andreas fault shows the extent of our discretized model fault plane. Stars denote hypocenters of 2004 and 1966 Parkfield earthquakes. (B) Interseismic slip velocity inferred from GPS data by Murray *et al.* (2001). We adopt this model of interseismic slip in our work. White dots denote relocated aftershocks from the 2004 earthquake (Langbein *et al.*, 2005). Hatched area denotes inferred locked asperity surrounded by aseismic creep.

the San Andreas fault (Segall and Du, 1993; Murray and Langbein, 2006). The streaks and patches of seismicity are thought to occur at the edges of locked patches that are bordered by creeping patches. Within these clusters at Parkfield, Nadeau and Johnson (1998) identified repeating earthquakes with nearly identical waveforms recurring with a period weakly proportional to the moment. Segall and Harris (1986) and Murray *et al.* (2001) inverted geodetic data sets for interseismic slip rates on the Parkfield section (Fig. 1B) and found that the locked section of the fault to the southeast extends into the region of the fault bordered by the patches of seismicity, providing further evidence for the locked asperity.

In this article we conclude that postseismic deformation following the 2004 Parkfield earthquake occurs predominantly as afterslip within the aseismically creeping part of the San Andreas fault surrounding the locked asperity. We utilize the continuous GPS network at Parkfield to investigate the frictional behavior on the San Andreas fault by developing a three-dimensional (3D) rate- and state-dependent friction model of afterslip. We show that a model for afterslip on the San Andreas fault at Parkfield governed by rate- and state-dependent friction is consistent with postseismic deformation recorded with the local network of continuous

GPS instruments, and we determine a range of frictional parameters that reproduce the observations.

Numerical models utilizing rate- and state-dependent friction laws show that transition zones from stable to unstable frictional sliding produce complex slip behavior including spontaneous generation of silent slip events (e.g., Liu and Rice, 2005; Shibazaki and Iio, 2003; Yoshida and Kato, 2003). Indeed, silent slip transients have been inferred within the transitional zone of the San Andreas fault near Parkfield (e.g., Gao *et al.*, 2000). The numerical models require the input of several frictional parameters estimated from laboratory experiments. However, relatively few studies have attempted to directly compare field measurements with the proposed frictional laws in order to estimate the frictional parameters for natural faults. Previous attempts by Stuart and Tullis (1995) to test frictional laws at Parkfield, California, with numerical models and interseismic geodetic and seismic data during the period between the 1966 and 2004 earthquakes concluded that the frictional parameters are not well resolved by the nearly constant interseismic deformation rates. This problem can be overcome using the nonsteady, rapid deformation following the 2004 earthquake, which is the purpose of our study.

Data and Observations

Data

Locations of 13 continuous GPS sites collecting data at 1 Hz (Langbein and Bock, 2004) and the coseismic and postseismic deformation measurements are displayed in Figure 2. The blue arrows and 95% confidence ellipses show the cumulative displacements during the first 9 months after the earthquake. The red arrows and 95% confidence ellipses show the coseismic offsets.

Positions were estimated for the Parkfield GPS sites every second for 45 min before and after the earthquake to obtain coseismic offsets using the techniques described by Larson *et al.* (2003) and augmented with modified sidereal filtering (Choi *et al.*, 2004).

Common-mode errors were minimized by stacking positions from sites outside the Parkfield region (Wdowinski *et al.*, 1997; Bilich *et al.*, 2004). The coseismic offsets are defined as the difference of the average positions 100 sec before the earthquake and the average positions 50–150 sec after the earthquake. The uncertainties differ significantly between the two components: the one standard deviation formal error is 1.5 mm for the east component and 3.0 mm for the north component.

We use the U.S. Geological Survey (USGS) continuous GPS automatic-processing results for the Parkfield area (http://quake.wr.usgs.gov/research/deformation/gps/auto/ParkfieldContin/) for the postseismic deformation period. The positions are in an ITRF2000-NA-fixed reference frame. We did not remove any outliers or common-mode noise in the data.

Observations

The amount of postseismic deformation following the Parkfield earthquake is relatively large. The cumulative 9-month postseismic displacements are at least twice as large as the coseismic offsets (Fig. 2). Langbein *et al.* (2006) show that moment release of modeled afterslip at Parkfield after 9 months exceeds that of the coseismic moment. This observation contrasts with observations from other earthquakes where the postseismic displacements in the first year after
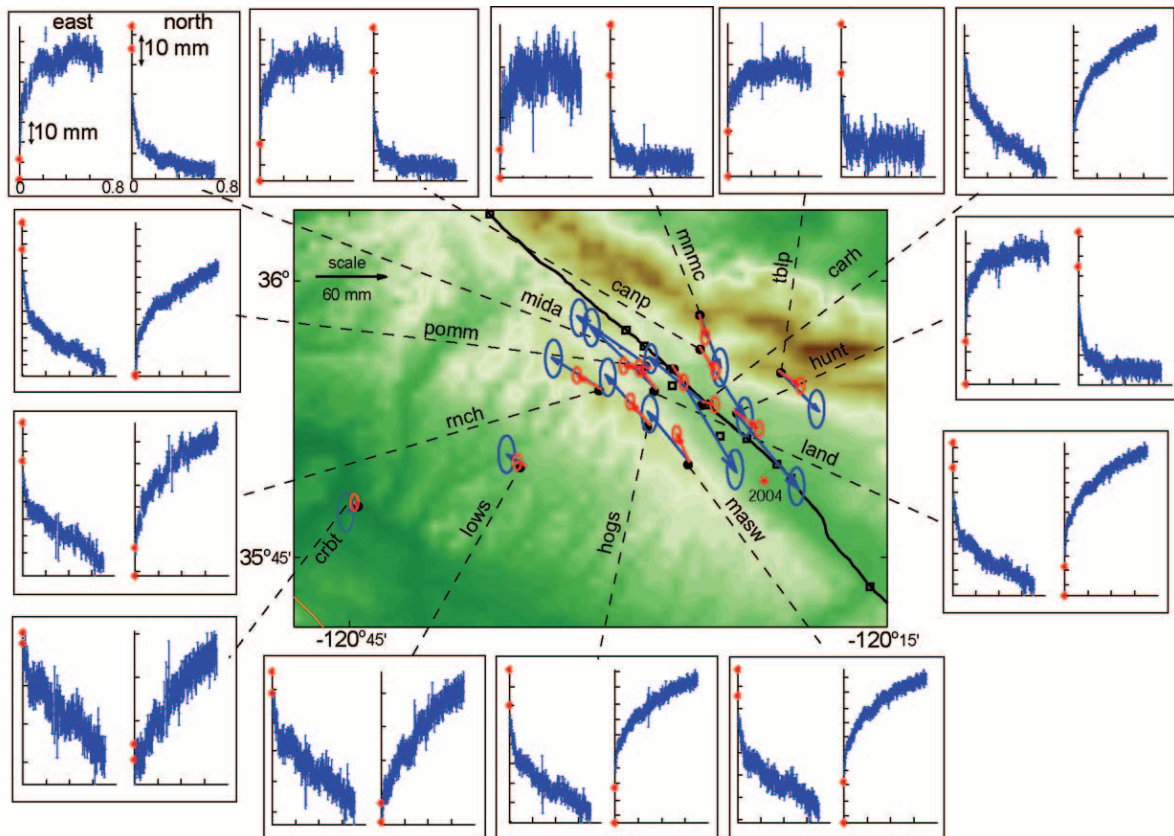

Figure 2. Locations of the 13 continuous GPS sites used in this study and the data. Blue arrows and 95% error ellipses show 9 months cumulative postseismic (including interseismic) displacements measured with GPS. Red arrows and 95% confidence ellipses show coseismic offsets determined from high-frequency GPS measurements. Time-series plots show east and north positions in millimeters with time in years after the earthquake. Each vertical tic represents 10 mm. Red dots on zero-time axis show positions immediately before and after the earthquake.

the earthquake are considerably smaller than the coseismic offsets. For example, the measured first-year cumulative postseismic displacements following the 2002 M_w 7.9 Denali fault, Alaska, earthquake are less than 0.15 m and on average less than 25% the size of the coseismic offsets (e.g., Hreins-dottir *et al.*, 2003; Pollitz, 2005; Freed *et al.*, 2006). Similar observations were made for the 1999 Izmit, Turkey, earthquake (e.g., Reilinger *et al.*, 2000; Ergintav *et al.*, 2002) and the 1999 M_w 7.6 Chi-Chi, Taiwan, earthquake (e.g., Yu *et al.*, 2001; Hsu *et al.*, 2002). Models of the postseismic deformation processes for each of the larger earthquakes indicate that a large contribution to the surface displacements comes from continued slip on the fault or distributed viscous flow at depths greater than the depth of the coseismic rupture.

A rough idea of the relative depths of coseismic and postseismic deformation might be obtained through a comparison of the spatial wavelengths of coseismic and postseismic surface displacements. Following Saint Venant's Principle (e.g., Fung, 1965), we know that the wavelength of surface deformation increases with depth to the source. The postseismic deformation following the 2004 Parkfield earthquake displays a pattern of surface displacements with shorter spatial wavelength than the coseismic displacements. We deduce this from a comparison of displacements at different times as a function of distance perpendicular to the fault. Figure 3 shows the coseismic displacements, the cumulative displacements after the first 24 hr following the earthquake, and the cumulative displacements after the first 9 months following the earthquake. Interseismic displacements were removed assuming a constant velocity given by the average velocities before the earthquake. It is clear, especially within 10 km of the fault, that the wavelength of the coseismic deformation field is longer than that of the postseismic periods. Unlike the postseismic displacements, the coseismic displacements within 5–10 km of the fault are insignificantly smaller than the coseismic displacements within 5 km. This suggests the coseismic slip was concentrated at greater depth than the source of postseismic deformation.

The time-series plots in Figure 2 show a period of rapid deformation for the first 0.1 year after the earthquake and lower rates of deformation at later times. The postseismic velocities at the end of the 9-month period have not returned to the interseismic rate, although we do not show the interseismic rate here. The coseismic offsets are shown in the time-series plots with two red dots at time zero. The dots show the positions just before and after the earthquake determined from the high-rate GPS data as described previously.

Eleven creepmeters along the Parkfield segment record surface deformation within a zone less than 20 m wide across the surface trace (Fig. 4) (Langbein *et al.*, 2005). The creepmeters measure extension at an oblique (~30°) angle to the fault, and the extension is converted to displacement parallel to the fault. The logarithmic shape of the displacement
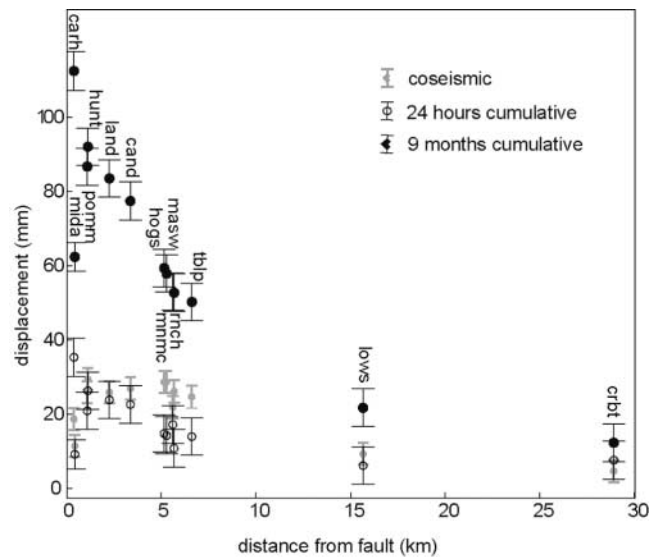

Figure 3. Plot of GPS displacements with distance perpendicular to the fault at different time periods. Interseismic deformation was removed from the postseismic signal assuming a constant velocity at each site given by the average velocity before the earthquake.

curves resembles the GPS time-series curves. The creepmeters at most sites show no clear offsets or extension during the earthquake, and surface creep commenced between 0.5 and 2 hr after the earthquake (Langbein *et al.*, 2005). This is consistent with the observation of lack of surface rupture immediately after the earthquake (Langbein *et al.*, 2005). At least one creepmeter installed by the University of Colorado shows sudden extension during the earthquake, but this is likely a recording of elastic strain above the buried coseismic rupture tip since surface rupture at this site was observed no earlier than four days after the earthquake (Bilham, 2005). A close look at the creepmeter data (Fig. 4) reveals that the logarithmic creep curves are actually comprised of small, discrete slip events, each evolving in time with similar, and smaller logarithmic slip patterns. The smaller slip events are clearest at sites xgh1 and crr1 in Figure 4.

Mechanisms of Postseismic Deformation

The suite of available geodetic observations supports the hypothesis that the postseismic deformation signal is dominated by shallow afterslip on the San Andreas fault. The creepmeters show up to ~15 cm of offset at the surface trace of the fault during the first several months after the earthquake. Our analysis of the GPS data at different time intervals along profiles perpendicular to the fault (Fig. 3) shows that the deformation is more localized after the earthquake than during the earthquake, consistent with shallow afterslip on the fault.

Analysis of postseismic deformation following other earthquakes shows that at least two other mechanisms in
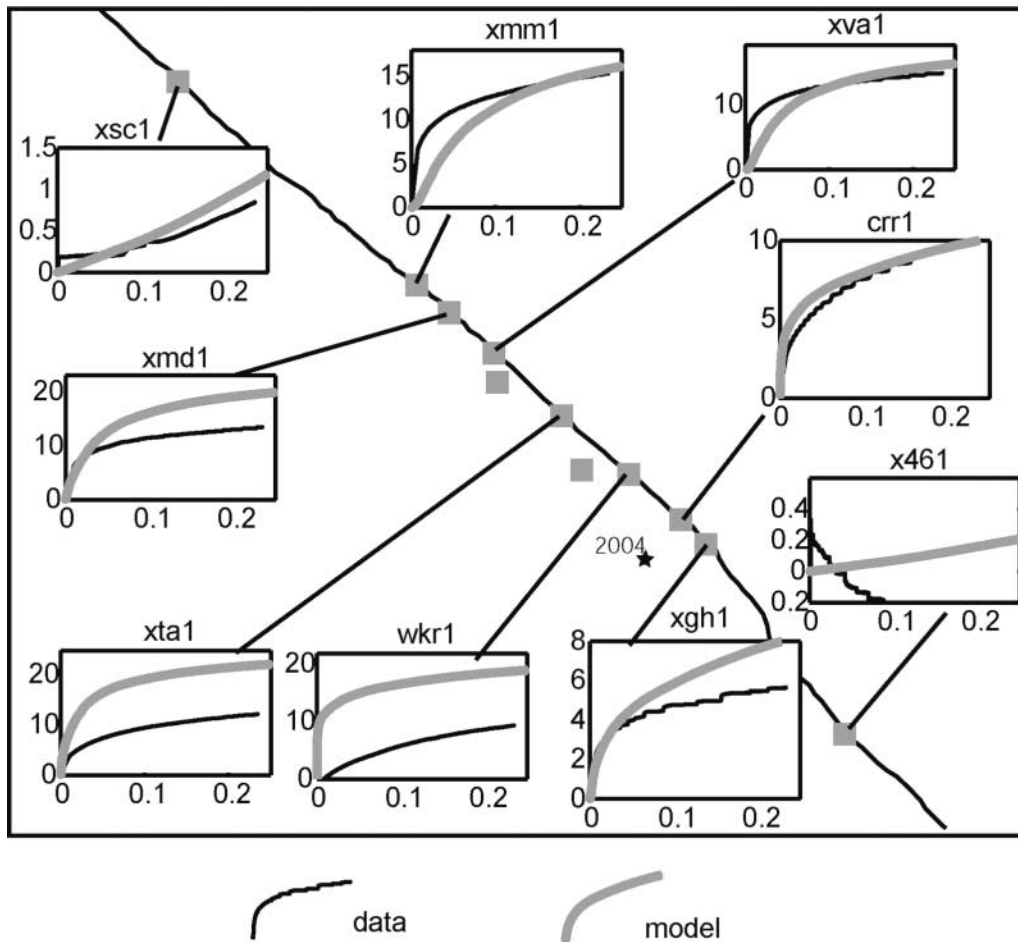
Figure 4. Locations of creepmeters and plots of offset with time following the Parkfield earthquake (thin black curves). Also shown (heavy gray curves) is a comparison with model cumulative surface slip (see results section). Vertical axes denote displacements in centimeters and horizontal axes denote time in years.

addition to afterslip can contribute substantially to the postseismic deformation signal. For example, analyses of the 1992 Landers and 1999 Hector Mine earthquakes show that the postseismic deformation can be explained with combined mechanisms of poroelastic flow and afterslip (Peltzer *et al.*, 1998) or poroelastic flow and distributed viscous flow in the upper mantle (Masterlark and Wang, 2002). Freed and Bürgmann (2004) and Pollitz *et al.* (2001) show that the postseismic deformation following the Hector Mine earthquake can be explained with distributed nonlinear viscous deformation in the upper mantle. Jonsson *et al.* (2003) demonstrate that the postseismic deformation signal following two June 2000 **M** 6.5 earthquakes in the south Iceland seismic zone is dominated by poroelastic flow.

We examined simple models of poroelastic and viscoelastic deformation processes at Parkfield to investigate the potential contributions to the surface deformation field. We modeled distributed viscoelastic deformation in the lower crust assuming the fault is embedded in a 15-km-thick elastic plate overlying a linear Maxwell viscoelastic substrate. The distributed viscous flow with viscosities as low as 10^{17} Pa sec results in cumulative surface displacements less than 10 mm, a small fraction of the observed total cumulative displacements. To investigate the possible contribution from fluid flow in the crust, we calculated the fully drained poroelastic deformation field (e.g., Jonsson *et al.*, 2003). The contribution from poroelastic deformation is negligible, with maximum cumulative displacements of <1 mm.

Based on these results, we feel it is reasonable to ignore viscoelastic and poroelastic deformation mechanisms and assume the postseismic deformation signal of the first 9 months results entirely from afterslip on the fault plane. As discussed below, laboratory experiments show that slip on faults at low temperatures, corresponding to depths less than 15 km, is described by a frictional process that depends on the rate of sliding and the state of asperity contacts on the fault surface. The purpose of this article is therefore to model postseismic deformation following the Parkfield earthquake as frictional afterslip on the San Andreas fault.

Previous Afterslip Studies

Previous investigations of afterslip inferred from geodetic observations have typically utilized either kinematic inversions for slip on a fault or fitting GPS or creepmeter time series with functional forms derived from proposed constitutive laws. In kinematic inversions, geodetic data are inverted for the spatial and temporal patterns of slip on the fault. The inversions are kinematic in the sense that fault slip is estimated without regard for the physics governing slip. We discuss the findings of some of these studies to set the context for this study.

Kinematic Slip Inversions

Kinematic inversions for afterslip following large strike-slip earthquakes show that afterslip often occurs over larger areas than the coseismic rupture, extending far below the region of coseismic rupture. For example, Bürgmann *et al.* (2002) and Hearn *et al.* (2002) show that much of the afterslip following the 1999 Izmit, Turkey, earthquake occurred below the coseismic rupture. These inferences are easily reconciled with a relatively simple model for strike-slip fault behavior in which the frictionally unstable part of the fault at depths between about 4 and 12 km ruptures during earthquakes and loads the deeper, frictionally stable part of the fault that slips rapidly to relax the load (e.g., Tse and Rice, 1986; Lapusta *et al.*, 2000). This model is based on laboratory experiments that demonstrate a temperature (depth) dependence on frictional stability (e.g., Blanpied *et al.*, 1995).

Yet, patterns of aseismic slip have been observed that are inconsistent with this simple model. For example, inversions of deformation following several large dip-slip earthquakes show afterslip at typically seismogenic depths (Hsu *et al.*, 2002 [Chi-Chi, Taiwan, earthquake]; Miyazaki *et al.*, 2004 [2003 Tokachi-oki, Japan earthquake]; Yagi *et al.*, 2003 [1994 Sanriku-haruka-oki earthquake in Japan]). Aseismic creep at seismogenic depths has also been inferred from studies of interseismic deformation.

Bürgmann *et al.* (2005) demonstrate that perhaps 75% of the Kamchatka subduction zone interface at seismogenic depths creeps aseismically between earthquakes. Igarashi *et al.* (2003) infer locked patches surrounded by aseismic creep on the subducting interface in northeastern Japan. Similar slip behavior is inferred at Parkfield where aseismic slip occurs at typically seismogenic depths. The heterogeneity in slip behavior on faults may reflect spatial heterogeneity in frictional properties.

While kinematic slip inversions provide insight into the location and magnitude of afterslip, the inversions provide no direct information on the physics governing afterslip. Furthermore, the usefulness of the kinematic inversions is limited by the fact that the inversions are nonunique and slip is poorly resolved at depths greater than a few kilometers (e.g., Bos and Spakman, 2003). To avoid these limitations, one can introduce a constitutive law governing the slip on the fault.

Mechanical Models for Afterslip

Laboratory experiments show that friction between small sliding blocks of rock is a function of slip velocity and one or more state parameters characterizing the state of asperity contacts. These so-called rate- and state-dependent friction laws (or rate–state friction) have been widely implemented in numerical models of fault slip during the earthquake cycle (e.g., Tse and Rice, 1986; Rice, 1993; Lapusta *et al.*, 2000). The Dieterich–Ruina rate-state friction formulation is

$$\tau = \sigma\left\{\mu + A\ln\frac{V}{V*} + B\ln\frac{V*\theta}{d_c}\right\} \qquad (1)$$

$$\frac{d\theta}{dt} = 1 - \frac{V\theta}{d_c}, \qquad (2)$$

where τ is shear stress on the fault, σ is the normal stress, V is sliding velocity, $V*$ is a reference velocity, μ is the nominal coefficient of friction at the steady reference velocity, θ is a state variable that evolves with time, A and B are laboratory-derived constants, and d_c is the so-called critical slip distance, which is interpreted as an indication of the size of asperity contacts and is thought of as the slip necessary to renew surface contacts. In this formulation, the state, θ, can be interpreted as the average asperity contact time because it increases linearly with time at zero slip velocity.

If θ does not vary with time, equations (1) and (2) reduce to the simpler steady-state expressions:

$$\tau_{ss} = \sigma\left\{\mu + (A - B)\ln\frac{V}{V*}\right\} \qquad (3)$$

$$\theta_{ss} = \frac{d_c}{V}. \qquad (4)$$

For slip at a constant velocity, friction evolves towards steady state (equation 3). For $A > B$, friction evolves to a higher value when the velocity increases and for $A < B$, friction evolves to a lower value. These conditions are referred to as velocity strengthening and velocity weakening, respectively. Velocity-strengthening portions of a fault are nominally stable, that is, they do not spontaneously rupture, although large stress perturbations can initiate unstable slip. Velocity-weakening portions of a fault can undergo spontaneous rupture under appropriate conditions (e.g., Ruina, 1983; Gu *et al.*, 1984).

Marone *et al.* (1991) introduced an approximate rate–state friction solution for shallow afterslip following large earthquakes. The afterslip zone is modeled with a spring and block slider. The spring, with stiffness *k*, is suddenly loaded

by the earthquake with stress, τ_c. It is assumed that the acceleration phase occurs during the earthquake and decelerating afterslip is governed by the steady-state equation (3). This is equivalent to assuming $B = 0$. This steady-state assumption is valid under certain conditions that we discuss in the Appendix.

Tse and Rice (1986) and Lapusta *et al.* (2000) implemented rate-state friction in numerical simulations of the earthquake cycle on two-dimensional (2D) strike-slip faults. Recently, the observations of periodic silent slip events at subduction zones has lead to the development of numerical simulations of the nucleation of accelerated slip events with rate- and state-dependent friction (Shibazaki and Iio, 2003; Liu and Rice, 2005). While there have been numerous applications of rate–state friction to the study of nucleation of earthquakes and silent slip events, the application to observations of afterslip following large earthquakes has received less attention. Marone *et al.* (1991) used the steady-state approximation to model creepmeter measurements of shallow afterslip following the 1966 Parkfield and 1987 Superstition Hills earthquakes. Linker and Rice (1997) used the same approximation to model deep afterslip following the Loma Prieta earthquake. They recognized that this approximation, which gives a nonlinear viscous behavior, is particularly relevant for deep afterslip at elevated temperatures below seismogenic depths as laboratory experiments show that the evolution of θ is negligible at high temperatures. They accordingly termed this approximation "hot friction." More recently, Hearn *et al.* (2002) used the hot friction approximation to model afterslip following the 1999 Izmit. Turkey, earthquake.

Montesi (2004) formulated a generalized power-law relaxation law for a spring-slider system for postseismic fault creep in which the rate–state steady-state approximation is a special case. As in Marone *et al.* (1991), Montesi (2004) fit the functional forms of the relaxation law to postseismic time-series observations from several large earthquakes.

Rate–State Afterslip Model for Parkfield

Model Setup for Parkfield

To model afterslip at Parkfield, we discretize a 65-km-long segment of the San Andreas fault into rectangular patches of uniform slip dislocations in a homogeneous elastic half-space (Fig. 1). We assume the slip rate distribution on the fault prior to the earthquake is that estimated by Murray *et al.* (2001), who inverted GPS velocities averaged over 1991–1998 for the interseismic slip rate. Also, following Murray *et al.* (2001), we assume the fault is locked down to 15-km depth to the southeast of Parkfield, creeping at 25 mm/yr down to 15-km depth northwest of Parkfield, and creeping at 32 mm/yr everywhere below 15-km depth. These large creeping sections of the fault are assumed to extend infinitely along the strike of the San Andreas fault.

Based on the lines of evidence summarized in the intro-

duction, we envision that the area of the fault bounded by the microseismicity (Fig. 1) is locked between earthquakes and is surrounded by aseismic fault creep. The locked part of the fault ruptures during the earthquake and creep in the surrounding areas accelerates to relax the coseismic stress load. We assume the coseismic stresses relax during afterslip according to equations (1) and (2) together with the equation relating stress on the fault to slip,

$$\dot{\tau} = G\dot{u} - \eta\ddot{u} - \dot{\tau}_0, \qquad (5)$$

where the dot denotes differentiation with respect to time, u is slip, τ_0 is the background stress, η is a radiation damping term introduced by Rice (1993) to approximate elastodynamic effects that prevent slip velocities from becoming unbounded, and $\mathbf{G}$ is a matrix that relates stress rate on a patch to slip rate on all patches. We construct $\mathbf{G}$ using the solution for an elastic dislocation in a homogeneous half-space (Okada, 1985). $\dot{\tau}_0$ is the stressing rate due to steady slip on the creeping parts of the fault outside of the 65-km-long discretized section, including steady slip on the San Andreas below 15-km depth (Fig. 1). We acknowledge that there is an inconsistency in our modeling of the interseismic stressing rate and the assumed interseismic slip distribution. Because we are assuming the interseismic slip rate from a kinematic inversion, we do not know the corresponding stressing rate on the fault that leads to this distribution. The preferable and proper approach would be to specify a far-field stressing rate on the fault and solve for the interseismic slip distribution. However, the accumulated interseismic stresses are small compared to the coseismic stress change, so it is reasonable to model the early postseismic period this way.

To solve the coupled equations (1), (2), and (5), we must specify values for $\sigma\mu$, σA, σB, d_c, and initial values for θ, V, and τ. Therefore the problem of estimating the afterslip distribution becomes the problem of determining the appropriate frictional parameters and initial conditions.

The typical approach in numerical studies (e.g., Rice, 1993; Lapusta *et al.*, 2000) has been to assume laboratory-derived values for A and B. Laboratory experiments suggest a temperature (and therefore depth) dependence (e.g., Blanpied *et al.*, 1995) with A–B positive (velocity strengthening) in the upper few kilometers, negative between about 4 and 12 km (where earthquake rupture typically occurs), and positive below about 12-km depth. This assumption is consistent with observations of slip behavior along many strike-slip faults and may be appropriate for the locked section of the San Andreas fault to the southeast of Parkfield, but it is an inappropriate model for the transition zone at Parkfield and the creeping section to the northwest. Therefore, we choose to estimate these parameters using the data from the 2004 earthquake. For simplicity, we assume these parameters vary linearly with depth and along strike, although more abrupt variations in frictional properties likely lead to abutting locked and creeping patches (e.g., Boatwright and Cocco,

1996). Furthermore, we assume the areas of the fault that creep after the earthquake are velocity strengthening. The nominal coefficient of friction, μ, is set to 0.6 in all the models in this article.

We estimate d_c and allow it to vary linearly with depth. It is not clear what value for d_c is appropriate for real faults or fault zones. Laboratory experiments on very small rock samples give distances of $\sim 10^{-5}$ m for d_c on smooth sliding surfaces. However, Marone and Kilgore (1993) established an experimental scaling relationship between d_c and fault-zone thickness that suggests d_c is on the order of $\sim 10^{-2}$ m for natural faults.

As a starting point, we will assume values of θ and τ before the earthquake given by the steady-state equations (3) and (4) at the assumed interseismic velocity (Fig. 1). As we demonstrate in the Appendix, this is a reasonable assumption if the areas on the fault that slip after the earthquake are velocity strengthening. This is clearly an oversimplification that must be improved upon in future work. For example, serpentine displays velocity-weakening behavior at high slip rates and velocity-strengthening behavior at low rates (Reinen *et al.*, 1994), so it is possible that areas of the fault that slipped during the earthquake continued to slip after the earthquake.

The Forward Model and Inversion for Rate-State Parameters

In order to estimate σA, σB, and d_c on the San Andreas fault near Parkfield, we design a forward model in which the change in shear stress on the fault resulting from coseismic slip drives rate–state frictional afterslip on the fault. We develop an inversion scheme to find the best-fitting frictional parameters by comparing the coseismic and postseismic observations with the forward model predictions.

Forward Model

We design a two-step forward model to invert for rate–state frictional parameters and coseismic and postseismic slip distributions. In the first step, we specify parameters discussed below for inverting the coseismic GPS data for the coseismic slip distribution. In the second step, we specify the rate–state friction parameters and initial conditions and solve for the evolution of afterslip as discussed above. The initial stress condition on the fault immediately after the earthquake is the sum of the coseismic stress change and the stress on the fault before the earthquake.

Coseismic Slip Estimation

The standard approach in kinematic inversions is to minimize the objective function

$$\Phi(\mathbf{s}) = \|\mathbf{d} - \mathbf{Gs}\|_2 + \gamma^2 \|\nabla^2 \mathbf{s}\|_2, \quad (6)$$

where $\mathbf{d}$ is the data vector, $\mathbf{s}$ is the vector of slips, $\mathbf{G}$ is the kernel matrix relating slip on the elastic dislocation to the surface displacements, $\|\nabla^2 \mathbf{s}\|_2$ is the Laplacian, γ is a weighting factor that controls the amount of smoothing, and $\| \|_2$ denotes the L-2 norm. However, it has been demonstrated (e.g., Bos and Spakman, 2003) that deep slip on the fault is poorly resolved with this approach. We have found a tendency for inversions to place large amounts of slip at depth to account for small misfits with the data because deep slip has a small influence on the sparsely distributed surface displacements. Furthermore, we have found that inversions with this method tend to allow small amounts of unresolvable slip to spread laterally over the entire fault. This spreading of small amounts of coseismic slip over large areas of the fault is problematic for the modeling of afterslip because the large areas of the fault that slip during the earthquake produce negative stress changes over much of the fault. These large areas with negative stress tend not to produce afterslip. To remedy these problems, we minimize a norm that penalizes slip that spreads out over the fault plane. We minimize the objective function

$$\Phi(\mathbf{s}) = \|\mathbf{d} - \mathbf{Gs}\|_2 + \gamma_1^2 \|\nabla^2 \mathbf{s}\|_2 + \gamma_2^2 \|\mathbf{Cs}\|_2, \quad (7)$$

where γ_1 and γ_2 are weighting factors and $\mathbf{C}$ is a compactness matrix defined as $C_{ij} = 1 + d_{ij}$ where d_{ij} is the distance from patch i to patch j.

The choice of weighting parameters, γ_1 and γ_2, is arbitrary, but because the evolution of afterslip depends strongly on the coseismic slip (stress) distribution, we can optimize the weighting parameters in our inversion of the coseismic and postseismic data. This is an advantage over standard kinematic slip inversions in which a statistical basis, such as trade-off curves or cross-validation, is utilized for selecting the weighting parameters. In kinematic slip inversions, the weighting parameter cannot be optimized directly from the data (e.g., Arnadottir and Segall, 1994).

In one set of inversions that we report in this article, we also include prior information on the slip distribution from a seismic slip inversion (Dreger *et al.*, 2005). To incorporate the prior, we minimize the objective function

$$\Phi(\mathbf{s}) = \|\mathbf{d} - \mathbf{Gs}\|_2 + \gamma_1^2 \|\nabla^2 \mathbf{s}\|_2 \\ + \gamma_2^2 \|\mathbf{Cs}\|_2 + \gamma_3^2 \|\mathbf{s} - \mathbf{s_p}\|_2, \quad (8)$$

where $\mathbf{s_p}$ is the prior slip distribution.

Afterslip Evolution. The second step in the forward model is the solution for the evolution of afterslip. As discussed previously, the afterslip evolution is completely determined with the specification of friction parameters $\sigma\mu$, σA, σB, and d_c, and initial conditions on state, stress, and slip rate. The initial conditions are taken to be the values immediately after the earthquake. Because the earthquake is modeled as an instantaneous event, the state parameter does not evolve and

the initial value for the state parameter is the same as the value before the earthquake. The preearthquake value for the state variable is approximated with equation (4) assuming the interseismic slip rate of Murray *et al.* (2001) (Fig. 1). The initial shear stress is the sum of the interseismic steady-state value from equation (3) plus the coseismic shear stress change. The initial slip rate is given by

$$V = V_0 \exp\left\{\frac{\Delta\tau}{\sigma A}\right\},$$

where V_0 is the preearthquake slip rate and $\Delta\tau$ is the coseismic shear stress change on the fault. This expression is obtained by substituting $\tau_0 + \Delta\tau$, where τ_0 is shear stress before the earthquake, for τ in equation (1), express τ_0 in terms of V_0 using equation (1), and solving for V, recognizing that θ does not change instantaneously.

Inversion for Rate-State Parameters

We invert the two-step forward model for the coseismic slip weighting parameters and rate–state frictional parameters that best fit the GPS data. In the inversions we allow σA, σB, and d_c to vary linearly with depth and along strike; however, we only report results in which the parameters vary with depth because we found that linear lateral variations did not significantly improve the fit to the data.

To invert the forward model, we find the global minimum of the misfit space using a downhill search method along coordinate directions with progressively decreasing step sizes. To be sure the minimum is indeed the global minimum and not a local minimum, we vary the starting point of the search a number of times until the global minimum is reproduced repeatedly.

Although it is insightful to know the best-fitting model, the inversion is incomplete without knowledge of the full parameter posterior probability distribution. An efficient and robust method to obtain the distribution is to sample with a Monte Carlo algorithm (e.g., Johnson and Segall, 2004), which requires tens or hundreds of thousands of forward model runs. At the time of this writing we have not run a full Monte Carlo inversion for the posterior distributions because of the large computational time required. Instead, we have coarsely sampled the probability distributions and estimated standard deviations assuming a Gaussian distribution. While the posterior distributions need not be Gaussian, this approach gives a rough estimate of the parameter distributions. We sample the posterior distribution of the model parameters, m,

$$\rho(m) = \mathbf{C} \exp\left\{-.5(\mathbf{d} - \hat{\mathbf{d}}(m))^T \Sigma^{-1} (\mathbf{d} - \hat{\mathbf{d}}(m))\right\}, \quad (9)$$

where $\mathbf{C}$ normalizes the distribution such that the integral over m is one, $\mathbf{d}$ is the data vector, is the vector of model displacements, and Σ is the covariance matrix. To sample the distribution, we vary each parameter m_i and invert for the best-fitting set of parameters $m_{j\neq i}$ using the downhill search method described previously. The 95% parameter confidence intervals reported in the Results section are taken from the Gaussian distribution that best fits the coarse sampling.

Results

We present four different analyses of the evolution of afterslip. In the first analysis we assume the entire fault has initial conditions on stress and state given by equations (3) and (4), as discussed previously. We show that these conditions do not reproduce the observations. We then present some kinematic slip inversions for afterslip to investigate the discrepancy between the first model and the observations. In the final two analyses, we alter the initial conditions on the fault to better reproduce the observations.

Kinematic Slip Inversions

We begin with kinematic slip inversions before examining the more complicated rate–state models. The kinematic inversions provide insight into the magnitude and location of afterslip that will guide our rate–state analysis. We invert for the cumulative afterslip for the first 24 hr and the first 9 months (Fig. 5). We remove an interseismic signal from the
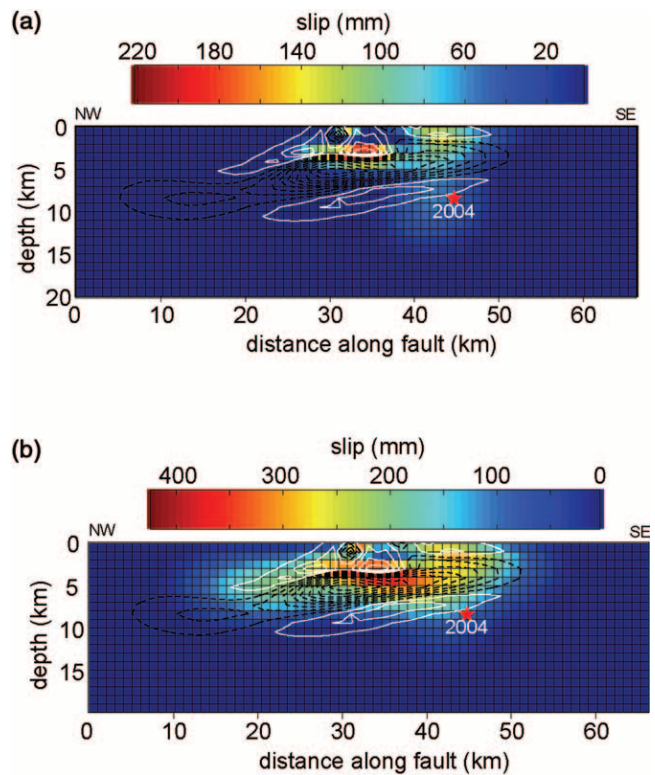

Figure 5.   Kinematic afterslip distributions. Contours of coseismic stress change: black denotes negative stress change, and white denotes positive stress change. (a) 24-hr cumulative afterslip; (b) 9-month cumulative afterslip.

total signal to isolate a postseismic signal. We subtract the accumulated displacements due to the average velocity at each site before the earthquake to isolate the postseismic signal. Note that we will not do this for the rate–state after-slip inversions because the interseismic slip is built into the solution. The inversions are conducted as described previously for the coseismic slip distribution. As mentioned previously, the weighting factor cannot be optimized from the data in the kinematic slip inversions. Therefore, we use the optimized coseismic weighting parameters obtained from the rate–state inversion discussed subsequently.

Figure 5 shows the cumulative afterslip after 24 hr and nine months. The contours show coseismic shear stresses induced by coseismic slip (estimated in the following rate–state inversion). The afterslip is localized in the upper 5 km after the first 24 hr. The afterslip is largely concentrated on areas of the fault that experience a shear stress increase due to slip deeper on the fault. In the following months, the afterslip spreads laterally and with depth and extends into the area of the fault that slipped during the earthquake. Figure 6 shows the fit to the 24-hr and 9-month cumulative displacements.

The slip below about 5-km depth is poorly resolved in the kinematic inversion. We show in the following analysis that this deeper slip may actually occur below the area of the fault that ruptured during the earthquake.

Rate-State Inversion

Figure 7 shows the best-fitting coseismic slip and afterslip distributions. The cumulative afterslip is shown after 24 hr and after 9 months (which includes the first 24-hr period). After 24 hr, the afterslip is highly localized within a roughly 5- to 10-km patch in the upper 5 km above the coseismic slip patch on the part of the fault that experienced the largest positive coseismic shear stress change. During the next 9 months, the afterslip spreads out laterally, above the coseismic rupture area, but the patch that slipped during the first 24 hr remains the patch with the largest amount of slip. A small amount of slip accumulates below 8 km after the first 24 hr. Figure 8 shows the accumulated displacements 9 months after the earthquake. The modeled 9-month cumulative surface displacements do not fit the data well. The misfit is particularly evident northeast of the fault where both the azimuth and magnitude of the displacements are inconsistent with the observations.

A feature of the rate–state slip distribution that is common to the kinematic slip inversion is the localization of afterslip in the upper 5 km, above the coseismic rupture. As in the rate–state model, the kinematic slip inversions show that the slip spreads out laterally after the first 24 hr. The largest discrepancy between the kinematic and mechanical models is the patch of slip in the kinematic inversion located between 0- and 6-km depth and between 40 and 50 km along strike. The rate–state model shows little afterslip on this area because this part of the fault was inferred to have slipped in
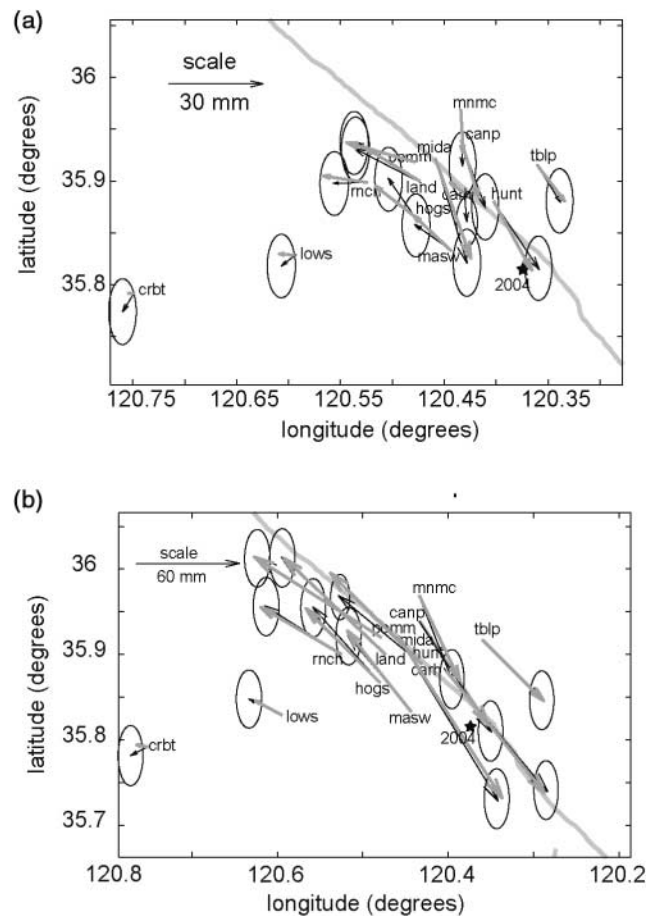

Figure 6. Fit to cumulative postseismic displacements from kinematic slip inversion (Fig. 5). Heavy gray arrows denote model displacements, and thin black arrows denote observed displacements. (a) 24-hr cumulative displacement; (b) 9-month cumulative displacement.

the coseismic model. This additional afterslip to the southeast in the kinematic inversion greatly improves the fit to the cumulative displacements (Fig. 6). The reduced χ^2 measure of misfit ($\chi^2 = \sum_i ((d_i - \hat{d}_i)/\sigma_i)^2/v$) where v is number of degrees of freedom) is 13.9 for the rate–state model and 0.97 for the kinematic inversion (χ^2 value near one indicates that the average misfit is about the size of the measurement errors). Note that the observed displacements in Figure 6b are slightly different than the observed displacements in Figure 8 because the accumulated interseismic displacements have been removed. Figure 5 superimposes contours of modeled coseismic shear stress change on the kinematic slip inversions. Most of the afterslip between 40 and 50 km occurs in a region of stress drop, which explains the lack of afterslip in the rate–state model. To generate more slip on this part of the fault with the rate–state model, we must alter the coseismic slip distribution, the frictional parameters, or the initial conditions on state, stress, or velocity.
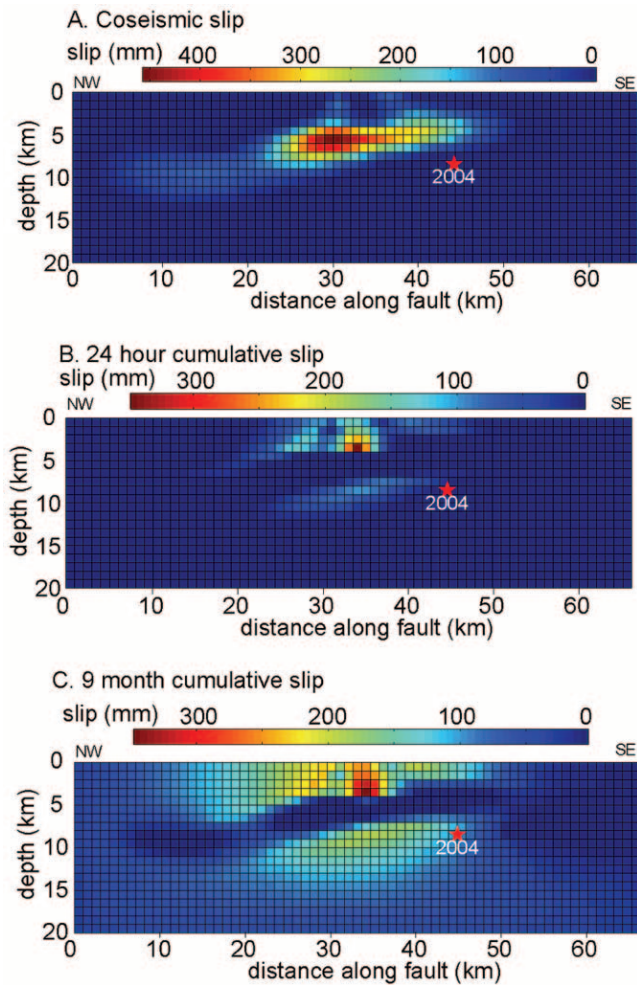
Figure 7.   Slip distributions for the best-fitting rate–state model with initial slip rates as shown in Figure 1B.
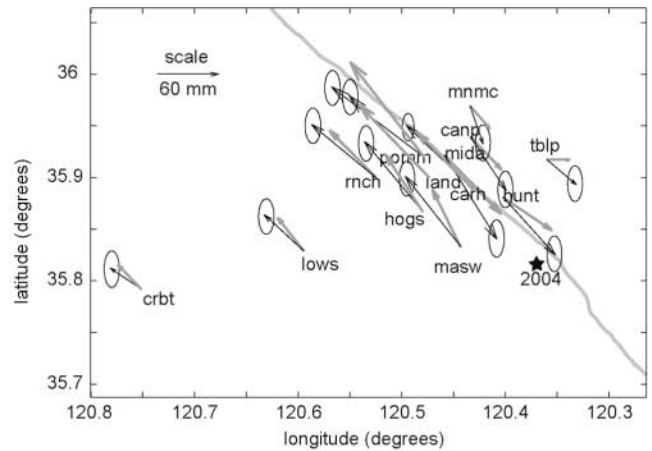

Figure 8.   The fit to 9 months cumulative displacements for the model shown in Figure 7. Heavy gray arrows show model displacements. Thin black arrows and 95% confidence ellipses show data and errors.
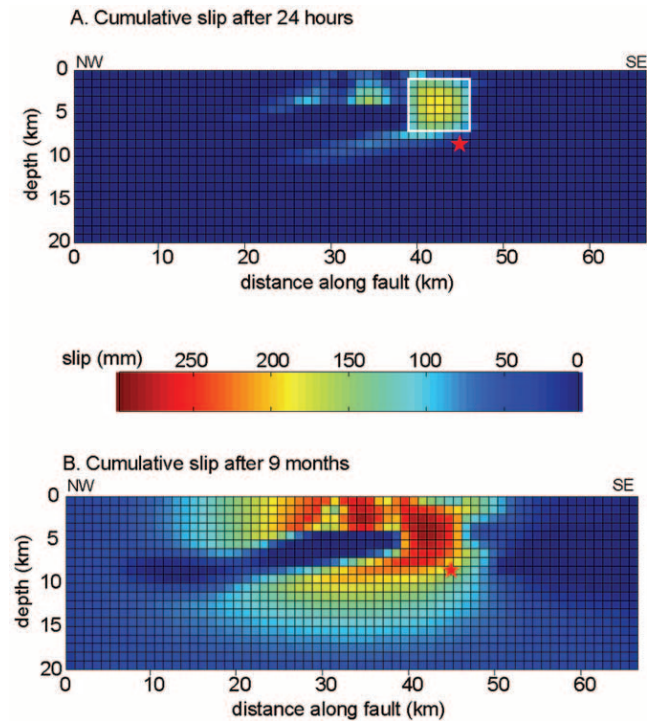

Figure 9.   Rate–state afterslip model with initially high slip rates between 0- and 6-km depth and 40–45 km from the end of the fault.

Rate-State Inversions with Altered Initial Conditions

High Initial Slip Speed. One way to produce more afterslip on the area of the fault within the white box in Figure 9A is to assume this part of the fault that ruptured coseismically continues to slip rapidly after the earthquake. We will assume initially high slip speeds within the white box in Figure 9A at the beginning of the evolution of afterslip and allow the slip to decelerate over the postseismic period. It is not clear what frictional conditions would allow this part of the fault to display dynamic rupture and continued rapid afterslip, but because we are not modeling the dynamics of rupture in this article, it is beyond the scope of our analysis to investigate the cause. We will simply assume for now that for some reason the afterslip on this part of the fault initiated during the recorded coseismic period (50–150 sec after the start of the earthquake).

We assume the initial slip rate in the box is the average slip rate over the 50- to 150-sec coseismic period recorded by the 1-Hz GPS data. We assume the stress on this part of the fault is the initial interseismic steady-state stress plus the coseismic stress change. The state parameter drops from the interseismic value to a smaller value during the earthquake, but because we are not modeling the dynamics of the earthquake, we do not know the state value at the end of the earthquake. Based on our experiments with the spring and slider models and trial and error, we prescribe the state value

immediately after the earthquake to be 1% of the preearth-quake value.

Figure 9 shows the 24-hr and 9-month cumulative af-terslip from the best-fitting rate–state model with initially high slip speeds in the designated box. Figure 10 shows the fit to the cumulative displacements. The addition of the large patch of afterslip in the white box does indeed improve the fit to the cumulative displacements. The χ^2 value for the fit to the 9-month cumulative displacements is 3.2 for this model, as compared to 13.9 for the first rate-state model. Figure 11 shows the fit to the GPS time series. We see that the model reproduces the rapid postseismic velocities during the first 0.1–0.2 years and the less rapid velocities during the later time periods. There is a tendency for the model to un-derfit the displacements at later times indicating that the model relaxes and returns to the preearthquake rate too quickly. This is particularly evident on the northeast side of the fault (Fig. 11) where the background velocity relative to stable North America is opposite in sign to the postseismic velocities. Note that in a stable North America reference frame, the interseismic velocities in this region are all di-rected to the northwest, whereas the accelerated right-lateral shear strain rate after the earthquake causes the motions on the North America side of the fault to be directed to the southeast. Here we can see that the slope of the modeled time-series changes sign prematurely. This might be an in-dication of an additional deformation process taking over at later times. For example, accelerated distributed viscous flow in the lower crust or upper mantle or accelerated slip below the 20-km-deep discretized fault zone might contrib-ute to the continued postseismic deformation signal.

Alternate Coseismic Slip Models and Heterogeneity in Fric-tional Parameters.　　Our coseismic slip distribution in Fig-ure 7A differs significantly from other slip estimates in the vicinity of the hypocenter. For example, the slip estimates of Dreger *et al.* (2005) and Liu *et al.* (2006) from seismic data and Johanson *et al.* (2006) derived from GPS and In-terferometric Synthetic Aperture Array (InSAR) measure-ments show more slip at the hypocenter and less slip at 5-km depth above the hypocenter, which is approximately the location of our slip discrepancy. It is possible that pushing the coseismic slip down to the depth of the hypocenter may generate a positive coseismic shear stress change in the area where we need to produce larger amounts of afterslip. Thus, we use the slip distribution of Dreger *et al.* (2005) as a prior on the slip in the vicinity of the hypocenter and invert for the coseismic slip using the objective function in equa-tion (8).

We found that this slightly improves the fit because more slip is generated above the hypocenter due to increased coseismic shear stress from slip at the hypocenter. However, this does not generate enough afterslip above the hypocenter to fit the data. It is clear that either the initial conditions or frictional properties on this patch above the hypocenter must be altered to produce the extra slip.
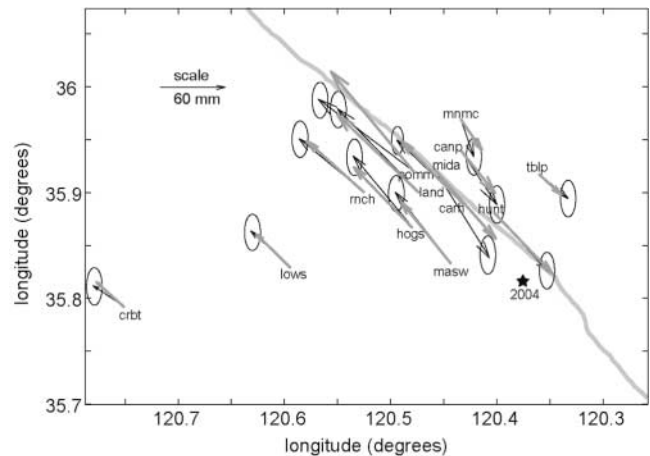

Figure 10.　　Fit to the cumulative postseismic dis-placements for the rate–state model with initially high slip rate in the designated region. Heavy gray arrows denote model displacements, and thin black arrows denote observed displacements.

We now allow the frictional parameters to be different inside and outside the white box in Figure 12A. We examine this possibility because test models show that reducing *A,* *A–B,* or d_c increases the moment release during the early afterslip period and, it is certainly logical to consider lateral heterogeneity in frictional parameters at Parkfield where we observe heterogeneity in slip behavior along strike. To main-tain the same number of unknowns as in previous inversions, we assume constant values for the frictional parameters over the fault inside and outside the white box. The inversion for frictional parameters is carried out as previously.

Figure 12 shows the best-fitting coseismic slip distri-bution, 9-month cumulative afterslip, and 9-month cumula-tive surface displacements. Assuming an effective normal stress on the fault of 50 MPa, $A = B = 0.001$ inside the white box, and outside the box $A = 0.002$ and $B = 0.0012$. d_c is 0.016 m everywhere on the fault. We see the patch of slip above the hypocenter in addition to the patch above the coseismic rupture. The fit to the cumulative 9-month dis-placements is an improvement over the first rate–state in-version ($\chi^2 = 4.2$ compared to $\chi^2 = 13.9$); however the inversion with the initially high slip speed fits the data slightly better ($\chi^2 = 3.2$).

The inversions suggest heterogeneity in frictional pa-rameters may be important for reproducing the postseismic observations at Parkfield. We note that heterogeneity in ini-tial conditions may also be an important factor that we have not explored fully to date. For example, increasing the initial shear stress on the fault would also increase the cumulative afterslip.

Comparison with Creepmeter Data

Figure 4 compares the creepmeter data for the first 0.3 years with the model cumulative slip at the surface. For clar-
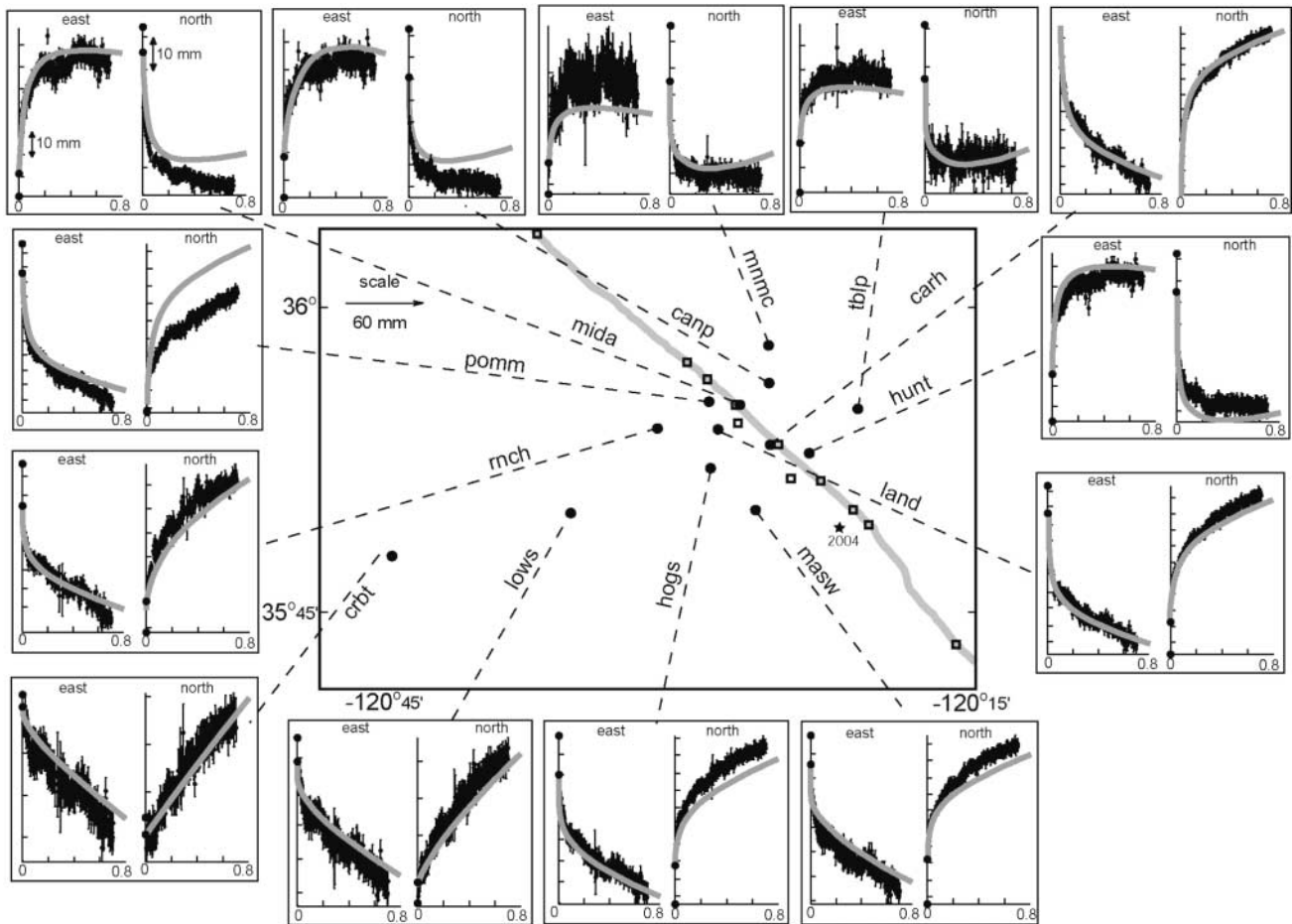
Figure 11.   Fit to the postseismic GPS time series. Black is data with 95% confidence intervals, and gray is model. Vertical axis is displacement in millimeters.

ity, we emphasize that we did not use the creepmeter data as a constraint in our inversions. The model tends to produce larger amounts of surface slip than inferred from the creepmeters. This overprediction may reflect the likely scenario that shear occurred over a broader zone than spanned by the creepmeters (<20 m). It has been shown repeatedly that strike-slip earthquakes produce shear across broad zones at the surface (e.g., Salyards *et al.*, 1992; Johnson *et al.*, 1994; Runnerstrom *et al.*, 2002). Besides, we actually model the average slip on 1- × 1-km patches, and therefore we do not expect to resolve highly localized, shallow deformation. What is clear from the comparison with the creepmeters is that the decay time of the data and model curves are comparable. We note that our model underpredicts the early rates of deformation at creepmeters xmm1 and xva1, unlike at the other locations where the early period model rates are faster or comparable to the observed rates. This may indicate that the model underpredicts the amount of afterslip to the northwest of the coseismic rupture. We also note that the model reproduces the prolonged acceleration at site xsc1, which contrasts with the other sites that show much shorter acceleration periods after the earthquake.

Estimates of Frictional Parameters

Table 1 shows the approximate 95% confidence intervals on the frictional parameters. Recall that we estimate σA and σB rather than determining σ independently of the frictional parameters. We therefore report values for A and B assuming an average effective normal stress of 50 MPa. The parameters σA, σB, and d_c vary linearly with depth, so we report the values at the center of the top and bottom rows of patches. A–B is on the order of 10^{-4} to 10^{-3}, which is about an order of magnitude lower than experimental values for granite at conditions well above or below the transition from potentially unstable (negative A–B) to nominally stable (positive A–B) friction (Blanpied *et al.*, 1995). It is also an order of magnitude lower than an estimate from an afterslip inversion of the Tokachi-oki, Japan, earthquake (Miyazaki *et al.*, 2004) and steady-state rate–state models of afterslip following other earthquakes (Linker and Rice, 1997; Hearn *et al.*, 2002). However, the estimated A–B values fall within a wide range of experimental values reported for serpentinite, which crops out along the San Andreas fault zone and is frequently mentioned as an important factor allowing for

A. coseismic slip distribution
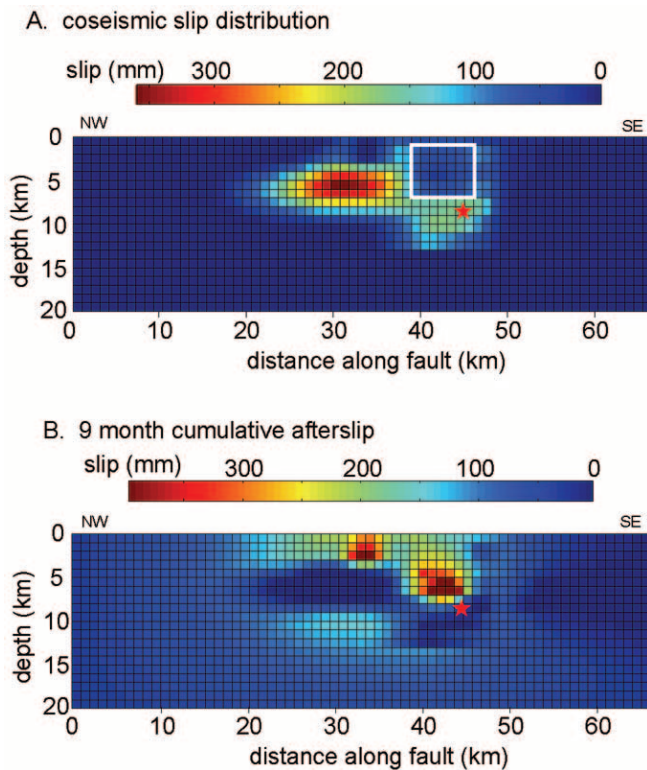

B. 9 month cumulative afterslip

Figure 12.　(A) Coseismic slip distribution with prior in the vicinity of the hypocenter from Dreger *et al.* (2005). (B) 9-month cumulative rate–state afterslip.

velocity-strengthening behavior of some faults (Reinen *et al.*, 1994). The low values of *A–B* might be indicative of a transition zone from velocity-weakening (negative *A–B*) to velocity-strengthening (positive *A–B*). Estimates of d_c are of the order 0.01–0.1 m corresponding to a fault gouge thickness of 1–10 m using the scaling relationship of Marone and Kilgore (1993).

Discussion

Two assumptions in our analyses of the frictional behavior of the Parkfield section of the San Andreas fault deserve further scrutiny. It is likely that the initial conditions on stress and state are not near steady-state conditions everywhere on the fault. We show in the Appendix that this assumption is valid for a limited range of frictional parameters. We show in Figure A2 that state and stress can vary significantly from the steady-state values when *A–B* is an order of magnitude lower than *A* and when d_c values are larger than ~0.05 m. However, our inversions suggest that *A–B* is an order of magnitude lower than *A* and d_c may be as large as 0.1 m. Therefore, in future modeling efforts we should relax the steady-state assumption.

The frictional conditions on the fault are likely more heterogeneous than we have assumed. It is clear that the frictional conditions must vary laterally from the locked sec-

tion to the southeast to the creeping section to the northwest. Furthermore, evidence that the Parkfield segment is comprised of locked patches surrounded by creeping sections (Nadeau *et al.*, 1995) indicates smaller-scale heterogeneity in frictional conditions. It has been shown (e.g., Lapusta *et al.*, 2000; Liu and Rice, 2005) that transition zones between locked and sliding can produce complex behavior. For example, Liu and Rice (2005) show that spontaneous slow slip events occur in the transition zone in their subduction models. It is likely that the transition in frictional properties at Parkfield leads to similar silent slip events inferred from geodetic data (e.g., Gwyther *et al.*, 1996) and modeled by Murray and Segall (2006). Indeed, we have shown in this analysis that heterogeneity in initial conditions or frictional parameters is necessary to fit the data.

We also note that the coseismic slip and afterslip distributions are at odds with seismicity observations (Langbein *et al.*, 2005) if we assume that aftershocks occur largely on areas of the fault that experience a shear stress increase from the earthquake. Most of the aftershocks in the depth range of 4- to 6-km depth lie within areas where the modeled shear stress was lowered by the earthquake. Unless the aftershocks respond to increased shear stress on small patches that did not slip within the broader area of coseismic rupture, this discrepancy suggests the coseismic slip is not correctly located. In these inversions we have used a homogeneous elastic half-space, ignoring the effects of vertical and lateral gradients in elastic moduli. Better agreement between locations of large coseismic stress increases and seismicity is achieved when we estimate the coseismic slip distribution assuming a layered elastic half-space because the coseismic slip (and therefore the patch of high shear stress above the slip) is several kilometers deeper than that found in the homogeneous earth inversion. Furthermore, we have ignored significant lateral variations in seismic velocity that are present across the San Andreas fault near Parkfield (e.g., Thurber *et al.*, 2004).

Conclusions

We have utilized coseismic and postseismic GPS data from the 2004 Parkfield earthquake to estimate rate–state frictional parameters on the San Andreas fault. We designed a two-step model to estimate coseismic and postseismic slip distributions and frictional parameters. In the first step of the forward model, we estimate the coseismic slip distribution from coseismic offsets obtained from 1-Hz GPS measurements. In the second step, the change in shear stress resulting from coseismic slip initiates afterslip, which is modeled with the Dieterich–Ruina formulation of rate–state friction. The Parkfield section of the San Andreas fault is discretized into 1- × 1-km dislocation patches in a homogeneous elastic half-space.

Assuming an effective normal stress of 50 MPa on the fault, we estimate *A–B* values on the order of 10^{-4}–10^{-3}, within a range of experimental values for serpentinite

Table 1
95% Confidence Intervals on Frictional Parameters

Parameter	Top of Fault	Bottom of Fault
A	0.0004–0.0052	0–0.024
B	0–0.0045	0–0.0468
$A–B$	0.0006–0.0018	0.0001–0.0021
d_c	0.020–0.250	0–0.650

(Reinen *et al.*, 1994) but about an order of magnitude lower than experimental values for granite at temperatures well above or below the frictional stability transition (Blanpied *et al.*, 1995). These low values for $A–B$ might indicate that afterslip occurred in a transition zone between velocity-weakening (negative $A–B$) and velocity-strengthening (positive $A–B$). The critical slip distance, d_c, is in the range 0.01–0.1 m, indicating a fault gouge thickness of 1–10 m using the scaling relationship of Marone and Kilgore (1993).

The best-fitting rate–state friction model with initial velocities given by the interseismic slip inversion of Murray *et al.* (2001) and steady-state values for stress and state is inconsistent with the GPS time-series data. We found that there needs to be significant afterslip on the fault above the hypocenter in order to fit the data. If we allow this area of the fault to slip with initially high slip rate at the initiation of the afterslip period, we can find an afterslip model that reproduces most of the postseismic GPS data. Alternatively, we can produce more afterslip on this part of the fault by lowering the values of A and $A–B$ or increasing the initial shear stress on the fault and using a coseismic model with higher slip near the hypocenter as suggested by other studies. The rate–state models reproduce the high surface velocities in the early postseismic period and the lower rates at later times. However, the modeled slip rate on the fault returns to the preearthquake rate earlier than the surface velocities, indicating either a deficiency in the afterslip model or indicating a second deformation process contributing to the deformation at later times.

Acknowledgments

References

Arnadottir, T., and P. Segall (1994). The 1989 Loma Prieta earthquake imaged from inversion of geodetic data, *J. Geophys. Res.* **99,** no. B11, 21,835–21,855.

Bilham, R. (2005). Coseismic strain and the transition to surface afterslip recorded by creepmeters near the 2004 Parkfield epicenter, *Seism. Res. Lett.* **76,** no. 1, 49–57.

Bilich, A., K. M. Larson, and P. Axelrad (2004). Techniques for reducing spatially-correlated errors in high-rate GPS positioning, *EOS Trans. AGU* **85,** no. 47, Fall Meet. Suppl., Abstract G53A–0110.

Blanpied, M., D. Lockner, and J. Byerlee (1995). Frictional slip of granite at hydrothermal conditions, *J. Geophys. Res.* **100,** no. B7, 13,045–13,064.

Boatwright, J., and M. Cocco (1996). Frictional constraints on crustal faulting, *J. Geophys. Res.* **101,** no. B6, 13,895–13,909.

Bos, A. G., and W. Spakman (2003). The resolving power of coseismic surface displacement data for fault slip distribution at depth, *Geophys. Res. Lett.* **30,** no. 21, doi 10.1029/2003GL017946.

Bürgmann, R., S. Ergintav, P. Segall, E. Hearn, S. McClusky, R. Reilinger, H. Woith, and J. Zschau (2002). Time-dependent distributed afterslip on and deep below the Izmit earthquake rupture, *Bull. Seism. Soc. Am.* **92,** no. 1, 126–137.

Bürgmann, R., M. G. Kogan, G. M. Steblov, G. Hilley, V. E. Levin, and E. Apel (2005). Interseismic coupling and asperity distribution along the Kamchatka subduction zone, *J. Geophys. Res.* **110,** B07405, doi 10.1029/2005JB003648.

Choi, K., A. Bilich, K. M. Larson, and P. Axelrad (2004). Modified sidereal filtering: implications for high-rate GPS positioning, *Geophys. Res. Lett.* **31,** L22608, doi 10.1029/2004GL021621.

Dieterich, J. (1992). Earthquake nucleation on faults with rate- and state-dependent strength, *Tectonophysics* **211,** 115–134.

Dreger, D. S., M. H. Murray, R. Nadeau, and A. Kim (2005). Kinematic modeling of the 2004 Parkfield earthquake, *Seism. Res. Lett.* **76,** no. 2, 211.

Ergintav, S., R. Bürgmann, S. McClusky, R. Cakmak, R. Reilinger, O. Lenk, A. Barka, and H. Özener (2002). Postseismic deformation near the Izmit Earthquake (17 August 1999, M 7.5) rupture zone, *Bull. Seism. Soc. Am.* **92,** no. 1, 194–207.

Freed, A. M., and R. Bürgmann (2004). Evidence of power-law flow in the Mojave desert mantle, *Nature* **430,** 548–551.

Freed, A. M., R. Bürgmann, E. Calais, J. Freymueller, and S. Hreinsdottir (2006). Implications of deformation following the 2002 Denali, Alaska earthquake for postseismic relaxation processes and lithospheric rheology, *J. Geophys. Res.* **111,** no. B1, B01401, doi 10.1029/2005JB003894.

Fung, Y. (1965). *Foundations of Solid Mechanics*, Prentice-Hall, Englewood Cliffs, New Jersey.

Gao, S., P. Silver, and A. Linde (2000). Analysis of deformation data at Parkfield, California: detection of a long-term strain transient, *J. Geophys. Res.* **105,** no. B2, 2955–2967.

Gu, J. C., J. R. Rice, A. L. Ruina, and S. T. Tse (1984). Slip motion and stability of a single degree of freedom elastic system with rate and state dependent friction, *J. Mech. Phys. Solids* **32,** no. 3, 167–196.

Gwyther, R., M. Gladwin, M. Mee, and R. Hart (1996). Anomalous shear strain at Parkfield during 1993–94, *Geophys. Res. Lett.* **23,** no. 18, 2425–2428.

Hearn, E., R. Bürgmann, and R. Reilinger (2002). Dynamics of Izmit earthquake postseismic deformation and loading of the duzce earthquake hypocenter, *Bull. Seism. Soc. Am.* **92,** no. 1, 172–193.

Hreinsdottir, S., J. T. Freymueller, H. J. Fletcher, C. F. Larsen, and R. Bürgmann (2003). Coseismic slip distribution of the 2002 M_w 7.9 Denali fault earthquake, Alaska, determined from GPS measurements, *Geophys. Res. Lett.* **30,** no. 13, doi 10.1029/2003GL017447.

Hsu, Y., N. Bechor, P. Segall, S. Yu, and K. Ma (2002). Rapid afterslip following the 1999 Chi-Chi, Taiwan earthquake, *Geophys. Res. Lett.* **29,** doi 10.1029/2002GL014967.

Igarashi, T., T. Matsuzawa, and A. Hasegawa (2003). Repeating earthquakes and interplate aseismic slip in the northeastern Japan subduction zone, J. Geophys. Res. **108,** no. B5, doi 10.1029/2002JB001920.

Johanson, I. A., E. J. Fielding, F. Rolandone, and R. Bürgmann (2006). Coseismic and postseismic slip of the 2004 Parkfield earthquake from space-geodetic data, Bull. Seism. Soc. Am. **96,** no. 4B, S269–S282.

Johnson, K., and P. Segall (2004). Viscoelastic earthquake cycle models with deep stress-driven creep along the San Andreas fault system, *J. Geophys. Res.* **109,** B10403, doi 10.1029/2004JB003096.

Johnson, A., R. Fleming, and K. Cruikshank (1994). Shear zones formed along long, straight traces of fault zones during the 28 June 1992 Landers, California, earthquake, *Bull. Seism. Soc. Am.* **84,** no. 3, 499–510.

Jonsson, S., P. Segall, R. Pedersen, and G. Bjornsson (2003). Post-earthquake ground movements correlated to pore-pressure transients, *Nature* **424,** no. 6945, 179–183.

Langbein, J., and Y. Bock (2004). High-rate real-time GPS network at Parkfield: utility for detecting fault slip and seismic displacements, *Geophys. Res. Lett.*, **31,** doi 10.1029/2003GL019408.

Langbein, J., R. Borcherdt, D. Dreger, J. Fletcher, J. Hardebeck, M. Hellweg, C. Ji, M. Johnston, J. Murray, R. Nadeau, M. Rymer, and J. Treiman (2005). Preliminary report on the 28 September 2004, M 6.0 Parkfield, California earthquake, *Seism. Res. Lett.* **76,** no. 1, 10–26.

Langbein, J., J. Murray, and H. A. Snyder (2006). Coseismic and initial postseismic deformation from the 2004 Parkfield, California, earthquake, observed by Global Positioning System, creepmeters, and borehole strainmeters, *Bull. Seism. Soc. Am.* **96,** no. 4B, S304–S320.

Lapusta, N., J. R. Rice, Y. Ben-Zion, and G. T. Zheng (2000). Elastodynamic analysis for slow tectonic loading with spontaneous rupture episodes on faults with rate- and state-dependent friction, **105,** no. B10, 23,765–23,789.

Larson, K. M., P. Bodin, and J. Gomberg (2003). Using 1-hz GPS data to measure deformations caused by the Denali fault earthquake, *Science* **300,** no. 5624, 1421–1424.

Linker, M., and J. Rice (1997). Models of postseismic deformation and stress transfer associated with the Loma Prieta earthquake, in *The Loma Prieta, California Earthquake of October 17, 1989: Aftershocks and Postseismic Effect*, P. A. Reasenberg (Editor), U.S. Geol. Surv. Profess. Pap. 1550-D, D253–D275.

Liu, Y., and J. Rice (2005). Aseismic slip transients emerge spontaneously in 3D rate and state modeling of subduction earthquake sequences, *J. Geophys. Res.* **110,** B08307, doi 10.1029/2004JB003424.

Liu, P., S. Custòdio, and R. Archuleta (2006). Kinematic inversion of the 2004 **M** 6.0 Parkfield earthquake including an approximation to site effects, *Bull. Seism. Soc. Am.* **96,** no. 4B, S143–S158.

Marone, C., and B. Kilgore (1993). Scaling of the critical slip distance for seismic faulting with shear strain in fault zones, *Nature* **362,** 618–621.

Marone, C., C. Scholtz, and R. Bilham (1991). On the mechanics of earthquake afterslip, *J. Geophys. Res.* **96,** no. B5, 8441–8452.

Masterlark, T., and H. F. Wang (2002). Transient stress-coupling between the 1992 Landers and 1999 Hector Mine, California, earthquakes, *Bull. Seism. Soc. Am.* **92,** 1470–1486.

Miyazaki, S., P. Segall, J. Fukuda, and T. Kato (2004). Space time distribution of afterslip following the 2003 Tokachi-oki earthquake: implications for variations in fault zone frictional properties, *Geophys. Res. Lett.* **31,** doi 10.1029/2003GL019410.

Montesi, L. (2004). Controls of shear zone rheology and tectonic loading on postseismic creep, J. Geophys. Res. **109,** doi 10.1029/2003 JB0002925.

Murray, J., and J. Langbein (2006). Slip on the San Andreas fault at Parkfield, California, over two earthquake cycles and the implications for seismic hazard, *Bull. Seism. Soc. Am.* **96,** no. 4B, S283–S303.

Murray, J. R., and P. Segall (2006). Spatiotemporal evolution of a slip-rate increase on the San Andreas fault near Parkfield, *J. Geophys. Res.* (in press).

Murray, J., P. Segall, P. Cervelli, W. Prescott, and J. Svarc (2001). Inversion of GPS data for spatially variable slip-rate on the San Andreas fault near Parkfield, *Geophys. Res. Lett.* **28,** 359–362.

Nadeau, R., and L. Johnson (1998). Seismological studies at Parkfield VI: moment release rates and estimates of source parameters for small repeating earthquakes, *Bull. Seism. Soc. Am.* **88,** 790–814.

Nadeau, R., W. Foxall, and T. McEvilly (1995). Clustering and periodic

recurrence of microearthquakes on the San Andreas fault at Parkfield, California, *Science* **267,** 503–507.

Okada, Y. (1985). Surface deformation due to shear and tensile faults in halfspace, *Bull. Seism. Soc. Am.* **75,** 1135–1154.

Peltzer, G., P. Rosen, F. Rogez, and K. Hudnut (1998). Poroelastic rebound along the Landers 1992 earthquake surface rupture, *J. Geophys. Res.* **103,** no. B12, 30,131–30,146.

Perfettini, H., and J.-P. Avouac (2004). Stress transfer and strain rate variations during the seismic cycle, *J. Geophys. Res.* **109,** doi 10.1029/2003JB002917.

Pollitz, F. F. (2005). Transient rheology of the upper mantle beneath central Alaska inferred from the crustal velocity field following the 2002 Denali earthquake, *J. Geophys. Res.* **110,** no. B8, B08407, doi 10.1029/2005JB003672.

Pollitz, F., C. Wicks, and W. Thatcher (2001). Mantle flow beneath a continental strike-slip fault: postseismic deformation after the 1999 Hector Mine earthquake, *Science* **293,** 1814–1818.

Reilinger, R., S. Ergintav, and R. Bürgmann (2000). Coseismic and postseismic fault slip for the 17 August 1999, M = 7.5, Izmit, Turkey earthquake, *Science* **289,** 1519–1524.

Reinen, L. A., J. D. Weeks, and T. E. Tullis (1994). The frictional behavior of Lizurdite and Antigorite Serpentinites: experiments, constitutive models, and implications for natural faults, *Bull. Seism. Soc. Am.* **143,** no. 1–3, 317–358.

Rice, J. (1993). Spatio-temporal complexity of slip on a fault, *J. Geophys. Res.* **98,** 9885–9907.

Ruina, A. (1983). Slip instability and state variable friction laws, *J. Geophys. Res.* **88,** 10,359–10,370.

Runnerstrom, E. E., L. B. Grant, J R. Arrowsmith, D. D. Rhodes, and E. M. Stone (2002). Displacement across the Cholame segment of the San Andreas fault between 1855 and 1893 from cadastral surveys, *Bull. Seism. Soc. Am.* **92,** no. 7, 2659–2669.

Salyards, S., K. Sieh, and J. Kirschvink (1992). Paleomagnetic measurement of nonbrittle coseismic deformation across the San Andreas fault at Pallett Creek, *J. Geophys. Res.* **97,** no. B9, 12,457–12,470.

Segall, P., and Y. Du (1993). How similar were the 1934 and 1966 Parkfield earthquakes? *J. Geophys. Res.* **98,** 4527–4538.

Segall, P., and R. Harris (1986). Slip deficit on the San Andreas fault at Parkfield, California, as revealed by inversion of geodetic data, *Science* **233,** 1409–1413.

Shibazaki, B., and Y. Iio (2003). On the physical mechanism of silent slip events along the deeper part of the seismogenic zone, *Geophys. Res. Lett.* **30,** no. 9, doi 10.1029/2003GL017047.

Stuart, W., and T. Tullis (1995). Fault model for preseismic deformation at Parkfield, California, *J. Geophys. Res.* **100,** no. B12, 24,079–24,099.

Thurber, C., S. Roecker, H. Zhang, S. Baher, and W. Ellsworth (2004). Fine-scale structure of the San Andreas fault zone and location of the SAFOD target earthquakes, *Geophys. Res. Lett.* **31,** doi 10.1029/2003GL019398.

Tse, S., and J. Rice (1986). Crustal earthquake instability in relation to the depth variation of frictional slip properties, *J. Geophys. Res.* **91,** 9452–9472.

U.S. Geological Survey, GPS automatic-processing results for the Parkfield area, http://quake.xr.usgs.gov/research/deformation/gps/auto/ ParkfieldContin/ (last accessed August 2006).

Wdowinski, S., Y. Bock, J. Zhang, P. Fung, and J. Genrich (1997). Southern California permanent GPS geodetic array: spatial filtering of daily positions for estimating coseismic and postseismic displacements induced by the 1992 Landers earthquake, *J. Geophys. Res.* **102,** 18,057.

Yagi, Y., K. Masayuki, and T. Nishimura (2003). Co-seismic slip, postseismic slip, and largest aftershock associated with the 1994 Sanriku-Haruka-Oki, Japan, earthquake. *Geophys. Res. Lett.* **30,** doi 10.1029/ 2003GL018189.

Yoshida, S., and N. Kato (2003). Episodic aseismic slip in a two-degree-of-freedom block-spring model, *Geophys. Res. Lett.* **30,** doi 10.1029/ 2003GL017439.

Yu, S. B., L. C. Kuo, and Y. J. Hsu (2001). Preseismic deformation and coseismic displacements associated with the 1999 Chi-Chi, Taiwan earthquake, *Bull. Seism. Soc. Am.* **91,** no. 5, 995–1012.

Appendix

Spring-Slider Model

To investigate the conditions under which it is appropriate to assume initial conditions for θ and τ given by equations (3) and (4), we construct a double spring and slider model to investigate the evolution of θ, τ, and V throughout periodic earthquake cycles (Fig. A1). Such zero-dimensional spring and slider models have been widely used to examine the fundamental behavior systems with rate–state friction (e.g., Ruina, 1983; Yoshida and Kato, 2003; Perfettini and Avouac, 2004). The sliders are pulled at a constant velocity of 0.01 m/yr and are connected by elastic springs. The frictional contact at the base of the slider is governed by the rate–state equations (1) and (2). Slider 1 is assigned velocity-weakening properties. Velocity-strengthening conditions are

Figure A1. Double spring-slider model governed by rate–state friction. The sliders are pulled at a constant rate of 0.01 m/yr. Slider 1 exhibits periodic earthquakes with velocity-weakening conditions, $A = 0.002$, $B = 0.004$. Slider 2 is assigned velocity-strengthening conditions, $A = 0.004$ and $B = 0.002$, and exhibits stable sliding throughout with rapid afterslip. d_c is 0.01 m for both sliders. Dashed lines in bottom plots are steady-state lines. t^- denotes time just before an earthquake and t^+ denotes time immediately after.

assigned to slider 2. So that slider 1 slips unstably, the spring on slider 1 is assigned a stiffness value less than the critical stiffness, k_c (e.g. Ruina, 1983). Slider 2 is assigned the same spring stiffness but is velocity strengthening ($A > B$) so it will slide stably. The spring stiffness, $k = 0.1k_c$, is chosen to approximate the effective stiffness of a circular fault patch with radius of about 10 km (Dieterich, 1992). Slider 1 is assigned $A = 0.002$, $B = 0.004$, and $d_c = 0.01$ m for all of the following numerical experiments. Slider 2 is assigned $A = 0.004$, $B = 0.002$, and $d_c = 0.01$ m for the plots in Figure A1, and these parameters are varied systematically in Figure A2. The normal stress on each slider is 300 MPa for all of the numerical experiments.

The rate–state equations (1) and (2) are coupled with the following force-balance equations for the two block sliders

$$\tau_2 = k_2(V_0 \delta t - u_2) - k_1(u_2 - u_1) - \eta \dot{u}_2 \quad \text{(A1)}$$

$$\tau_1 = k_1(u_2 - u_1) - \eta \dot{u}_1, \quad \text{(A2)}$$

where τ_i denotes the shear stress for slider i, u_i is the displacement of slider i, and η is the radiation damping term introduced in equation (5). We solve the system of nonlinear equations (10), (11), (1), and (2) with Matlab Ordinary Differential Equation solvers that utilize the Runge–Kutta formulas.

Figure A1 shows the slip and stress histories for the two sliders after many earthquake cycles. Between earthquakes, slider 1 is essentially locked and steadily builds up stress. Slider 2 slips continuously throughout the cycle. The coseismic slip on slider 1 loads slider 2. Slider 2 relaxes the coseismic load with rapid afterslip. Slider 2 creeps rapidly following the earthquake for a number of years and slows down to a nearly steady interseismic rate until the next earthquake. The bottom panels of Figure A1 plot the stress history as a function of slip rate (phase plots). The dashed lines show the steady-state stress as a function of slip rate (equation 3). The phase plot for slider 1 shows the characteristic phase orbits for unstable slip due to velocity weakening. The phase orbit for slider 2 shows that the deceleration of slip following the earthquake follows the steady-state line. This result, however, depends to some extent on the choice of frictional parameters for slider 2. We now examine the influence of the frictional parameters on the behavior of slider 2, which is our analog for an area of the fault displaying afterslip.

Figure A2 shows the stress, slip, and state histories for slider 2 for nine different sets of frictional parameters. The heavy gray lines show the shear stress, τ_2, state, θ_2, and displacement, u_2, as a function of time or slip rate. The dashed thin lines show the steady-state values (equations 3 and 4) for state and stress at the slip rate given by the solution to the mechanical system. As we stated previously, this is exactly how we choose the initial conditions on state and stress for the Parkfield earthquake, by calculating the values on the steady-state line at the interseismic slip rate deter-
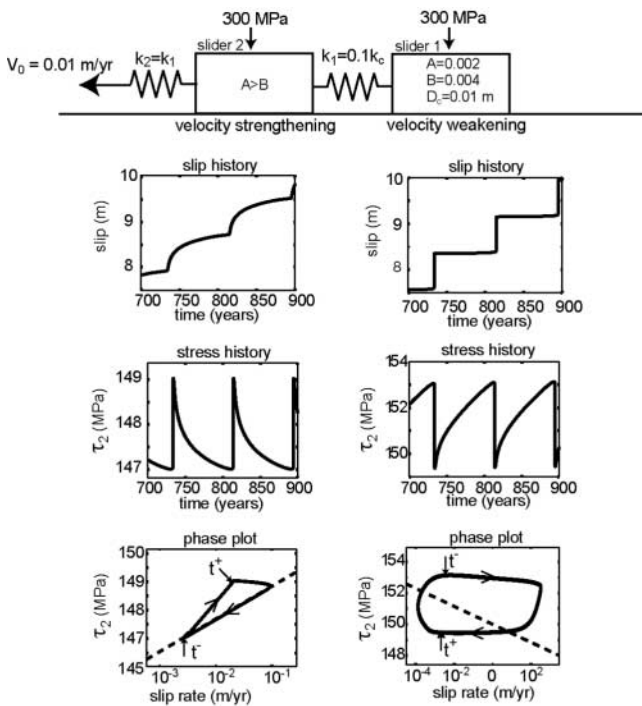
A. Vary A-B, A = 0.004 (fixed)

B. Vary stiffness, k (equivalently, fault size)
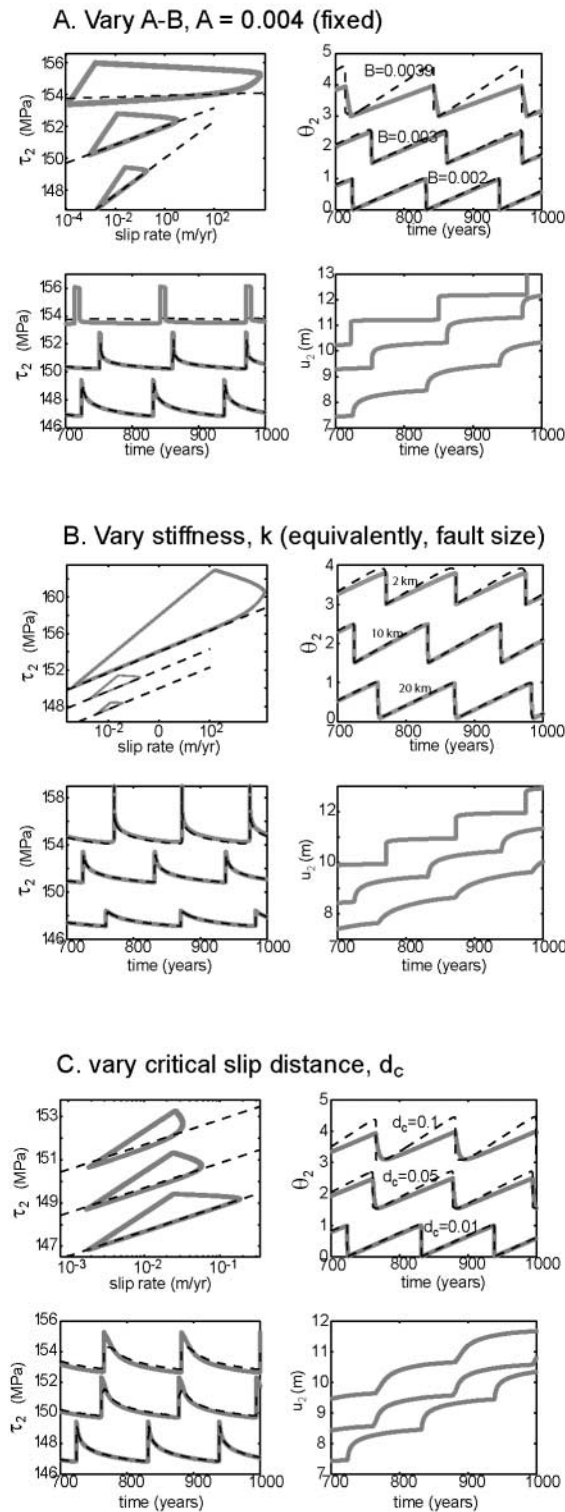

C. vary critical slip distance, d_c

Figure A2. Plots (heavy gray lines) of shear stress, τ_2, state, θ_2, and displacement, u_2, for slider 2, as well as phase plots and displacement history. Dashed lines show steady-state values (equation 3) at the corresponding model slip rate. In each plot $A = 0.004$, $B = 0.003$, and $d_c = 0.01$.

mined by Murray *et al.* (2001). When the heavy gray line is near the dashed thin line, equations (3), and (4) are a good approximation for state and stress. In Figure A2, part A, A is held fixed at 0.004 and B is varied. We see that the state and stress plot near the steady-state curves for A–B values on the order of the size of A but not when A–B is an order of magnitude smaller than A. We vary the stiffness of the spring in Figure A2, part B. The spring stiffness is analogous to the stiffness of the fault embedded in the elastic medium, which for a circular crack with radius, r, and elastic shear modulus, M, is

$$k = \frac{7\pi\mu}{24r} \qquad (A3)$$

(e.g., Dieterich, 1992). We see in Figure A2, part B that the state and stress plot near the steady-state curves for slip patches with radius larger than 2 km. Thus, because we are modeling slip patches that are at least 5–10 km in radius, we do not need to worry about the size of the slip patch violating the steady-state assumption for the initial conditions. Figure A2, part C shows that the state and stress plot near the steady-state curves for critical slip distances on the order of 0.01 m or less.

Summarizing the results from the numerical experiments, our assumption that the initial conditions for stress and state can be approximated by the steady-state equations (3), and (4) is valid for limited ranges in frictional parameters. Namely, for the assumption to be valid, A–B must be on the order of the size of A, and d_c must be on the order of 0.01 m or less. This may be problematic in areas of transition from velocity weakening (A–$B < 0$) to velocity-strengthening (A–$B > 0$) where A–B might be quite small. Furthermore, laboratory studies show that d_c scales with fault gouge thickness and may lie within the range 0.01–0.1 m for natural faults (Marone and Kilgore, 1993).

Department of Earth and Planetary Science
University of California
Berkeley, California 94720-4767
(K.M.J., R.B.)

Department of Geological Sciences
Indiana University
2002 E. 10th Street
Bloomington, Indiana 47405
(K.M.J.)

Department of Aerospace Engineering Sciences
University of Colorado
Boulder, Colorado 80309-0429
(K.L.)